OPEN ACCESS
Journal of Innovative Optical Health Sciences
Vol. 17, No. 1 (2024) 2350016 (10 pages)

DOI: 10.1142/S1793545823500165

World Scientific
www.worldscientific.com

Intravascular photoacoustic and optical coherence tomography imaging dual-mode system for detecting spontaneous coronary artery dissection: A feasibility study

Yongwei Wang[*,†], Yuyang Wan[*,†] and Zhongjiang Chen[‡,§,¶]
[*]*MOE Key Laboratory of Laser Life Science &*
Institute of Laser Life Science, South China Normal University
Guangzhou 510631, P. R. China

[†]*College of Biophotonics*
South China Normal University
Guangzhou 510631, P. R. China

[‡]*School of Medical Technology and Engineering*
Fujian Medical University
Fuzhou 350004, P. R. China
[§]*zjchen@fjmu.edu.cn*

Received 7 March 2023
Accepted 17 May 2023
Published 28 June 2023

In this work, we present an intravascular dual-mode endoscopic system capable of both intravascular photoacoustic imaging (IVPAI) and intravascular optical coherence tomography (IVOCT) for recognizing spontaneous coronary artery dissection (SCAD) phantoms. IVPAI provides high-resolution and high-penetration images of intramural hematoma (IMH) at different depths, so it is especially useful for imaging deep blood clots associated with imaging phantoms. IVOCT can readily visualize the double-lumen morphology of blood vessel walls to identify intimal tears. We also demonstrate the capability of this dual-mode endoscopic system using mimicking phantoms and biological samples of blood clots in *ex vivo* porcine arteries. The results of the experiments indicate that the combined IVPAI and IVOCT technique has the potential to provide a more accurate SCAD assessment method for clinical applications.

Keywords: Spontaneous coronary artery dissection (SCAD); intravascular optical coherence tomography (IVOCT); intravascular photoacoustic imaging (IVPAI).

[¶]Corresponding author.

1. Introduction

Spontaneous coronary artery dissection (SCAD) is a relatively rare but extremely serious condition that usually manifests as severe chest pain and acute hemodynamic damage.[1–4] SCAD remains an elusive and challenging clinical entity eight decades after its initial description.[5] Two hypotheses for the mechanism of SCAD have been proposed. The first is that intimal dissection allows blood from the lumen to penetrate the vessel wall, thereby creating a false lumen, and then an intramural hematoma (IMH) forms within the vessel wall, leading to the separation of its layers.[6–8] This inside-out hypothesis is the predominantly proposed mechanism in other vascular beds, including cervical artery dissection. The second and less well-known mechanism is the formation of an IMH within the arterial media occurring as the primary process, leading to a secondary intimal tear in some patients; this is the outside-in hypothesis.[9–12] IMH is present in many cases of SCAD, with the majority of them demonstrating IMH alone without intimal dissection.[13] SCAD has gained attention as a key cause of acute coronary syndrome and sudden cardiac death among women. Accurate diagnosis and treatment at an early stage of the disease are critical to patient survival. Emerging evidence suggests that the optimal short-term and long-term management strategies for women with SCAD differ substantially from those for women with atherosclerotic coronary disease.[14]

Recently, the clinical recognition of SCAD has increased because coronary angiography is utilized frequently in the clinical evaluation of patients with acute coronary syndromes. However, most angiographers are not familiar with angiographic variants of SCAD.[12] Coronary angiography is an imperfect technique because it utilizes a luminogram, and thus can only be used to examine blood vessels and not the coronary wall.[15] Owing to its limited resolution, cardiac computed tomography (CT) angiography is not recommended for ruling out SCAD, but its noninvasive nature renders it very attractive for assessing arterial healing, particularly in large and proximal coronary vessels.[16] Similarly, cardiac magnetic resonance imaging may be able to demonstrate hyperintensity areas within the vessel wall in patients with IMH. This technique avoids additional radiation exposure but, in most cases, lacks the required resolution for the diagnosis of SCAD.[5] Thus, accurate characterization of SCAD with these technologies remains challenging.[17–19] Intracoronary diagnostic techniques have provided a new window into the diagnosis of this elusive condition in patients presenting with the phenotype of intramural hematoma. Intracoronary imaging techniques such as intravascular optical coherence tomography (IVOCT) and intravascular ultrasound (IVUS), can provide detailed morphological information on coronary lesions and on the location of dissection planes between the different layers of the arterial wall, and have enabled a more detailed clinical assessment of SCAD.[20–23] However, the lumen–intimal interface is not as distinctly delineated as OCT due to the low resolution ($\approx 150\,\mu$m), which renders it inferior for visualizing intimal tears.[10,12] IVOCT is an optical imaging modality similar to IVUS. With its ultra-high axial resolution (5–20 μm) and high image contrast, the resolution of IVOCT is an order of magnitude higher than IVUS. Thus, IVOCT has become a more popular imaging tool for intravascular disease diagnosis in recent years. The depth penetration of optical coherence tomography depends on such factors as the sensitivity of the system, scattering, and absorption in the tissue.[24] In most cases, optical coherence tomography cannot completely reflect the adventitia of blood vessels, providing only incomplete information.[25–27] Intravascular photoacoustic imaging (IVPAI) is another emerging intravascular imaging technique. It can provide submillimeter resolution at penetration depths of up to a few millimeters.[28,29] However, IVPAI has a limited ability to image the subtle structures of blood vessels.[30] Due to cost constraints, most catheterization laboratories can only use one type of intracoronary technology for SCAD diagnosis.[12] We chose to combine IVOCT and IVPA into one system, and we found that that system can provide two types of two complementary information at the same time.

More and more multimodal intravascular imaging methods are proposed to diagnose the cardiovascular diseases. Wang *et al.* developed and combined PAI and ultrasound endoscope with a diameter of 1 mm that was assembled with a Ø25–Ø9-μm tapered fiber to achieve high-resolution deep-penetration imaging of lipid-rich plaque.[31] Furthermore, several tri-modality imaging systems have been recently reported.[30,32,33] Although these tri-modality imaging systems provide more complementary information to image the tissue, the

diameter of the probe is too large to achieve intravascular imaging. In addition, Xianjin Dai *et al.* described such a miniature endoscope only 1 mm in diameter that integrates photoacoustic imaging (PAI), optical coherence tomography (OCT), and ultrasound (US), but the probe needs to be fixed by three stainless steel tubes, and the assembly process is more complicated.[34] Ji Leng *et al.* developed a novel multi-spectral intravascular tri-modality (MS-IVTM) imaging system with a 0.9-mm miniature catheter, but they need to use expensive optical parameter oscillator laser as light source and the signal line of the probe's ultrasonic transducer needs to be bent too much.[35] Jianguo Ma *et al.* demonstrated a new design for a forward viewing fiber-scanning probe with reduced outer diameter.[36,37] But forward-viewing probes are better suited for imaging such as branches of the airways and the stomach or the bladder.[38] Side-viewing probes based on rotating fibers are suited for the imaging of tube-like hollow organs such as the coronary artery or the gastro-intestinal tract.[39,40] Although above imaging methods can be used to image vascular lesions, no one method was designed to resolve the SCAD based on the pathologic characteristics.

In this work, we present an intravascular dual-mode endoscopic system for recognizing SCAD by combining IVOCT with IVPAI, which utilizes a probe with an outer diameter of 1.0 mm. In the proposed dual-mode endoscopic system, IVOCT can provide excellent vascular anatomy information and superficial detection of IMH. IVPAI, which is based on the principle of optical absorption, can provide image information of IMH with high resolution, high contrast, and deep penetration. Thus, IVPAI can provide deep IHM information. The combination of these two technologies can provide complementary information at the same time to improve the efficiency of the diagnosis of SCAD and offers a good foundation for clinical treatment in the future. To our knowledge, this is the first application of combined optical coherence tomography and photoacoustic in the detection of SCAD.

2. Materials and Methods

The schematic illustration of the system is shown in Fig. 1(a). In our study, for the IVPAI, we used a quasi-continuous laser (DS20HE-1064D/R, Photonics, USA), which is a q-switched and pulses free

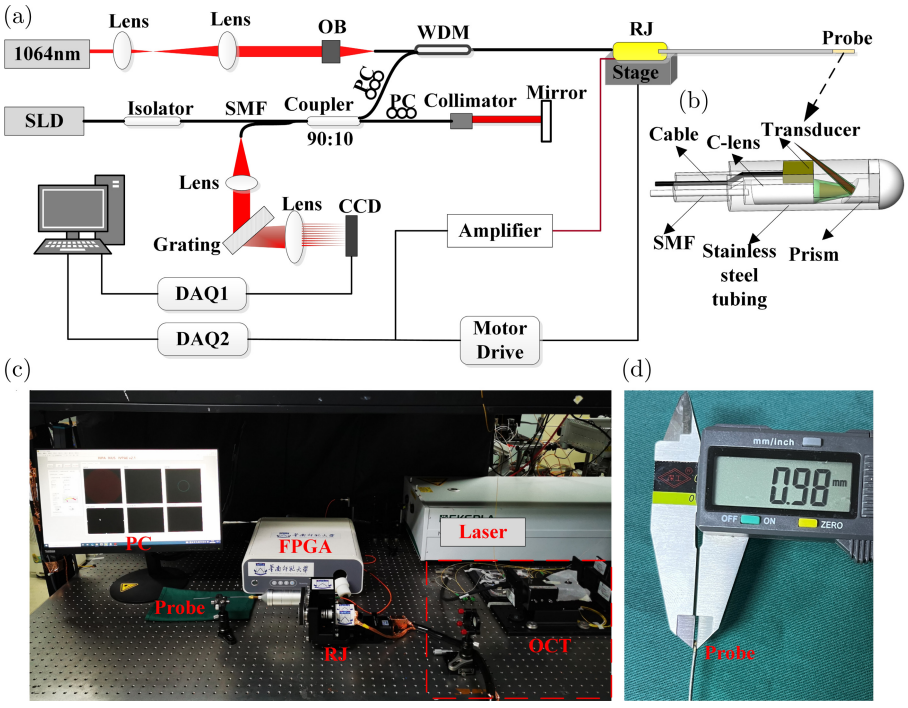

Fig. 1. (a) Schematic of the IVPAI and IVOCT dual-mode endoscopic system. 1064 nm: 1064 nm pulse laser, OB: objective lens, WDM: wavelength division multiplexer, RJ: rotary joint SLD, super luminescent diode, SMF: single mode fiber, PC: polarization controller, DAQ: data acquisition system CCD: charge-coupled device. (b) Architecture and photograph of the endoscopic probe. (c) Photo of part of the dual-mode system. (d) Photo of the endoscopic probe.

from intra-pulse modulation laser, as the light source to excite the photoacoustic signal. It has an output wavelength of 1064 nm with a pulse width of 22 ns, and its frequency is adjustable. Here, the frequency was set to 25 kHz as the intravascular light excitation source for IVPAI. We also applied a trigger signal from the laser as the main trigger to synchronize the IVOCT and IVPAI systems. The output laser beam was expanded by lens 1 ($f = 10$ mm) and lens 2 ($f = 30$ mm), and then coupled to one end of the customized wavelength division multiplexer (WDM) through a fiber coupling system. For the IVOCT, the light source was a broadband super luminescent diode (SLD1018S, Thorlabs, USA) with a maximum output power of 30 mW and a bandwidth of 45 nm centered at 1310 nm, which served as the light source for the IVOCT imaging system, corresponding to 17 μm theoretical axial resolution (in air). The super luminescent diode light source was connected to a single-mode fiber coupler through an optical isolator. The function of the optical isolator is to prevent the light reflected from the system then causing damage to the light source. Then the light was divided into the sample and reference arms by a fiber coupler such that 90% of the light energy would enter the sample arm and 10% would enter the reference arm. In the sample arm, the light from the 1064 nm laser and the light from the super luminescent diode were coupled into a beam of light through a wavelength division multiplexer (WDM), and were both connected to the sample arm. The rear end of the wavelength division multiplexer was connected to a single-mode fiber with a core diameter of 9 μm through a rotary joint (RJ) (MFO108, Moflon, China), and the RJ consisted of an optical slip ring and an electrical slip ring, both of which were coaxial. The RJ was fixed on a stepper motor scanning platform. The optical slip ring was connected to a stepper motor (PKP546N18B-L, Oriental Motor, Japan) to rotate the endoscopic probe. Another stepper motor was fixed on the platform to enable the endoscopic probe to be pulled back. The ultra-thin electronically controlled translation platform (MTS204 series, Beijing Beiguang Century Optoelectronics Co., Ltd., China) was used to provide a maximum roll back distance of 100 mm. The frame rate of the system image was 5 fps, and the rollback speed was set to 0.5 mm/s. The IVPAI excitation light and IVOCT detection light illuminated the tissue from the endoscopic probe. The probe was capable of simultaneous collection of IVPAI and IVOCT signals. The IVPA signals were detected by a single-element ultrasound transducer. After the photoacoustic signals were received by the ultrasonic transducer, it passed through the photoelectric slip ring system. Then, the photoacoustic signals were amplified with a low-noise amplifier (LNA-650, RFBAY, USA). Finally, the signals were digitized using a data acquisition (DAQ) card (PCI-5124, National Instrument, USA) with 12-bit resolution and a sampling rate of 200 MS/s. For the IVOCT, to optimize the axial resolution, two sets of fiber polarization controllers FPC561 (1260–1625 nm, Thorlabs, USA) were used for the sample and reference arms, respectively, to manage the polarization mode dispersion.[41,42] The light returned from the reference arm and the sample interfered at the No. 2 port of the fiber coupler, and then the interference signal was received by the self-made spectrometer. The output beam of the interference port fiber was collimated (AC254-050-C, Thorlabs, USA) and directed toward a transmission grating (1145 line/mm, Wasatch Photonics, USA). An achromatic lens with $f = 100$ mm (AC508-0100-C, Thorlabs, USA) focused the dispersed light onto a high-speed line scan charge-coupled camera (2048L InGaAs Linescan Camera, Sensors Unlimited, USA) at line rates up to 76 kHz with 2048 pixels. Data were streamed from the camera to an acquisition computer through a Camera Link interface card (PCIe-1433, National Instrument, USA). The acquisition, processing, and visualization of IVOCT and IVPAI images were done using LabVIEW and MATLAB.

In order to achieve both the miniaturization and multifunctionality of the probe, we designed and customized the dual-mode probe and assembled an endoscope probe that enables dual-mode imaging. The system can simultaneously provide information from the two complementary modes, reducing repeated testing of patients. Figure 1(b) shows a schematic of the intravascular dual-mode endoscope probe, which consisted of a single mode fiber, a C-lens, a prism, an ultrasound transducer, and a metal housing. To reduce back-reflection light, the cleaved fiber tip of the single mode fiber (SMF-28e+, Corning, USA) had an angle of 8°, and the proximal end of the C-lens was polished at angle of 8°. The C-lens had a diameter of 0.5 mm, a length of 1.45 mm, radius of curvature of 0.75, and a work distance of about 3.0 mm. The output beam from

the single mode fiber was focused by the C-lens, and then the focused beam was reflected by a rod mirror with a diameter of 0.5 mm at an angle of 55°. The C-lens and the prism were coaxially fixed using UV-curing optical adhesive in a metal housing with an outer diameter of 1 mm Fig. 1(d). The ultrasound transducer was also fixed in the metal housing. The photoacoustic signals were detected by a miniature single-element ultrasound transducer with a center frequency of around 40 MHz, a bandwidth of 40%, and a size of 0.55 mm × 0.45 mm × 0.2 mm, which provided high photoacoustic axial resolution. Figure 1(c) shows part of the dual-mode system.

3. Results

3.1. *System resolution*

To verify the lateral and axial resolutions of the IVPAI and IVOCT dual-mode system, a tungsten fiber with a diameter of 7 μm was selected as the target and fixed on a special sample holder. Figures 2(a) and 2(d) display the IVPAI and IVOCT images obtained by the system scanning the tungsten fiber. Figures 2(b) and 2(c) show the lateral and axial resolutions of IVPAI. The lateral and axial pixel widths were utilized as the line spread functions (LSPs) to evaluate the resolution. Based on the line spread functions, the lateral resolution of IVPAI was 64 μm, and its axial resolution was 25 μm. Figures 2(e) and 2(f) show the lateral and the axial resolutions of IVOCT. The lateral resolution of IVOCT was 17 μm, and its axial resolution was 18 μm.

3.2. *Phantom experiment*

The feasibility of the integrated dual-mode endoscopic imaging system was verified through a phantom experiment. The absorption peak of deoxyhemoglobin is at 920 nm, but since this wavelength needs to be realized by using an optical parametric oscillator (OPO) laser because the main component of IMH is blood. In order to provide the best possible imaging of the dissection, a long excitation laser wavelength should be chosen. We used 1064 nm for photoacoustic imaging. A 1064-nm laser can be used to excite the blood and generate photoacoustic signals.[43,44] The 1064 nm light source was used on an *ex-vitro* blood clot to verify its excitation efficiency and contrast, and the laser energy density was 50 mJ/cm^2, which is far lower than the safety threshold of 1 J/cm^2 listed in the American National Standards Institute laser safety

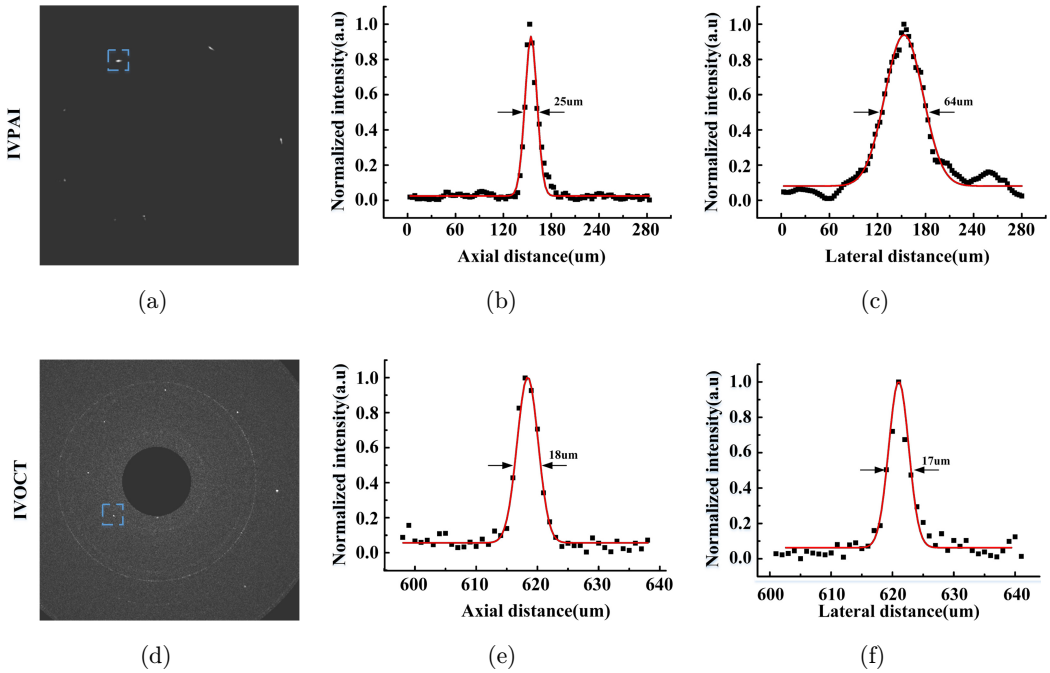

Fig. 2. (a) Cross-sectional image of the tungsten fiber acquired by IVPAI. (b) Lateral resolution of IVPAI. (c) Axial resolution of IVPAI. (d) Cross-sectional image of the tungsten fiber acquired by IVOCT. (e) Axial resolution of IVOCT. (f) Lateral resolution of IVOCT.

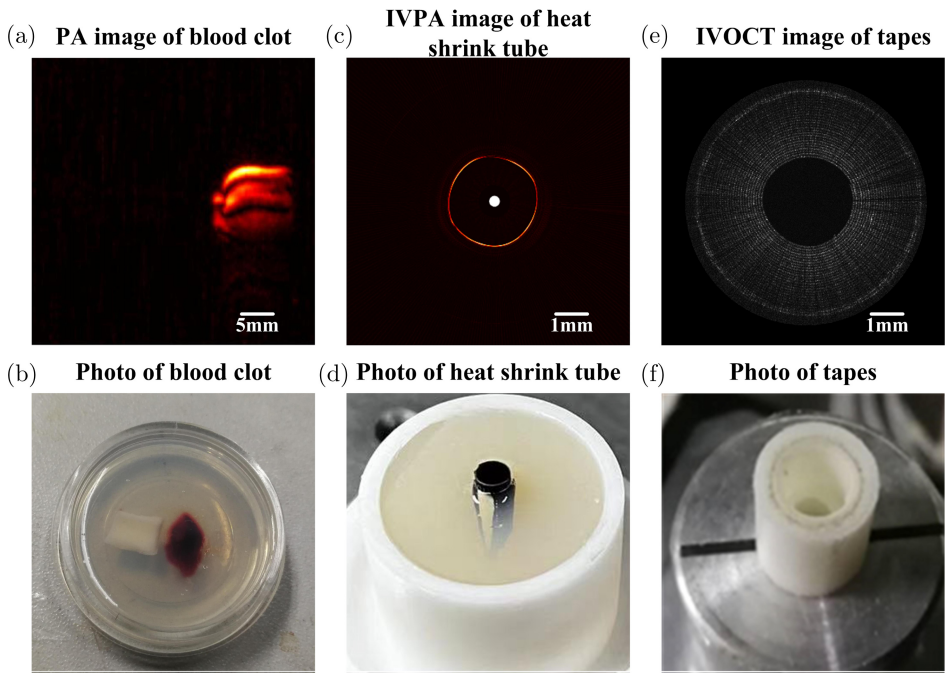

Fig. 3. System performance verification. (a) IVPAI image of vessel wall and blood clot at 1064 nm excitation. (b) Photo of the blood clot phantom. (c) Cross-sectional images of the black heat-shrinkable tube phantom acquired by IVPAI. (d) Photo of the black heat-shrinkable tube phantom. (e) Cross-sectional images of the white tape phantom acquired by IVOCT. (f) Photo of the white tape phantom.

standards.[45] Arterial blood from rabbit ears was taken with a medical needle and injected into a mold in line with the tiled artery sample and fixed with 3% agar to coagulate. Then, we used a flat scanning platform to scan the sample. As shown in Fig. 3(a), there were obvious differences in absorption between the blood vessel wall and blood clot. The 1064-nm laser has a high sensitivity to excitation through selective absorption, but the absorption of the blood vessel walls is very weak, so 1064 nm can be used as the excitation wavelength for the system. To verify the imaging capability of the IVPAI system, we used a black heat-shrinkable tube as a phantom to perform a ring scan, as shown Fig. 3(c). It can be seen from the results that the IVPAI was able to ring scan image the entire tube wall. The performance of the IVOCT system was tested by imaging a phantom that had been made by coiling translucent tape (Scotch, 3M, Saint Paul, U.S.) with a layer structure of $\approx 60\,\mu$m thickness around a plastic tube. As shown Fig. 3(e), the tail of the tape could be distinguished in the IVOCT image, as shown Fig. 3(c). Photos of the three phantoms are provided in Figs. 3(b), 3(d), and 3(f).

3.3. *Ex vivo porcine artery experiment*

To further demonstrate the capability of imaging biological tissues with the dual-mode endoscopic imaging system, the results of an *ex vivo* porcine artery experiment are shown in Fig. 4. According to the pathogenesis of SCAD, we prepared an *ex-vivo* phantom of SCAD.[46,47] Fresh rabbit blood was injected into different locations in normal porcine arteries and left to solidify into blood clots to simulate different types of IMHs. Blood was injected from the intimal surface to simulate intimal tear-type SCAD (inside-out) and from the adventitia to simulate IMH type SCAD (outside-in) by rupture of the vasa vasorum. Then the porcine arteries were fixed in 3% agarose gel. The probe was placed in the arterial lumen to create an intravascular imaging environment. As shown in Fig. 4(a), due to the excellent near-field resolution, IVOCT was able to accurately identify the precise location of an IMH caused by intimal tears, and it provided structural information about the vessel wall; the IMH has a "dark appearance" (low reflectivity), indicating low backscattering. Figure 4(b) shows the cross-sectional images of the porcine artery acquired by

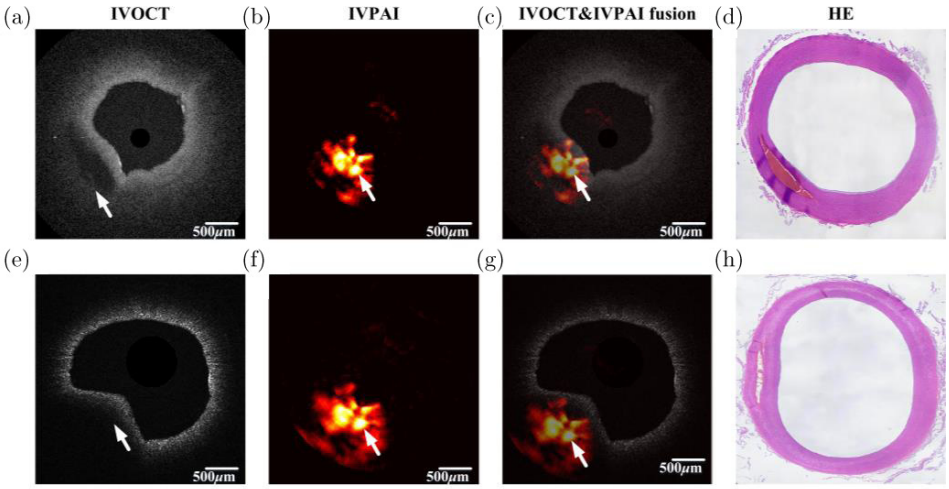

Fig. 4. *Ex vivo* IVPAI and IVOCT of a segment of a porcine artery: (a) Cross-sectional image of the inside-out type IMH acquired by IVOCT. (b) Cross-sectional image of the inside-out type IMH acquired by IVPAI. (c) IVPAI and IVOCT fusion image of inside-out type IMH. (d) Hematoxylin-eosin staining (HE) histological photograph of inside-out type IMH. (e) Outside-in type IMH image acquired by IVOCT. (f) Outside-in type IMH image acquired by IVPAI. (g) IVPAI and IVOCT fusion image of outside-in type IMH. (h) HE histological photograph of outside-in type IMH.

IVPAI, Superficial clots were also evident on IVPAI; the IMH has a "light appearance," indicating high absorption. Since the absorption of IMH at the excitation wavelength of 1064 nm is much larger than that of the blood vessel wall, only the image of the IHM can be displayed, but anatomical information about the vessel wall is missing. The IVPAI and IVOCT fusion image of the inside-out type IMH is shown in Fig. 4(c). As shown in Fig. 4(e), owing to the limited penetration depth of IVOCT into the vessel wall, the deep blood clots of phantom could not be visualized by IVOCT; however, as shown in Fig. 4(f), the deep clot of phantom could be recognized by IVPAI. As shown in Fig. 4(g), fusion of the IVPAI and IVOCT images of outside-in type IMH can provide a good complement to the shortcomings of the two different modes. Figures 4(d) and 4(h) show the corresponding histological photographs.

4. Discussion

We have developed an intravascular dual-mode endoscopic imaging system combining IVPAI and IVOCT. This system has a miniature probe with an outer diameter of 1.0 mm. We have demonstrated that system can image different types of IMHs *ex vitro* phantom. Because the vascular wall has strong scattering at 1310 nm, IVOCT can provide structural information about the vascular wall to indicate whether there is an initial tear. Owing to the limited imaging depth of IVOCT, an IMH formed by damaged adventitia cannot be detected by IVOCT, but it can be detected by IVPAI. Superficial IMHs can also be detected by IVPAI, but IVPAI cannot provide anatomical information about the normal blood vessel wall because there is no significant difference in absorption between blood and vessel wall at 1064 nm. Therefore, combining IVPAI and IVOCT has the potential to provide a more accurate assessment method for studying the disease mechanism of SCAD. Although the intravascular dual-mode endoscopic imaging system has been demonstrated that a feasible to detect spontaneous coronary artery dissection, some aspects of the system can be improved. First, the imaging speed of the system should be optimized to overcome the adverse effect of the pulses on imaging, which imaging speed need to over 16 frames per second.[48–50] Second, the sensitivity of the US transducer should be improved to increase the signal-to-noise ratio, for example, use a collinear catheter design, use dual-element or PMN-PT/Epoxy 1–3 composite ultrasonic transducer.[51–53] Third, to better satisfy clinical needs, the imaging performance of the system should be evaluated on human arterial dissection samples. Fourth, processing and engraving on the light-emitting end surface of the optical fiber realizes the transformation of multiple wavelengths

from Gaussian light to non-diffraction beam, thereby achieving the purpose of expanding the depth of focus, and then solving the contradiction between lateral resolution and imaging depth.[54,55]

5. Conclusions

In summary, our intravascular dual-mode IVPAI and IVOCT endoscopic imaging system validates the feasibility of detection of SCAD, and the combination of the two can provide structural information of different layers of IHM and blood vessels. This study shows that the system has the potential to provide a more accurate SCAD assessment method for clinical applications.

Acknowledgments

The authors acknowledge funding from the National Natural Science Foundation of China (NSFC) under grants 61627827, 61705068, the Natural Science Foundation of Fujian Province 2021J01813, and the Fujian Medical University Research Foundation of Talented Scholars XRCZX2021004.

Conflicts of Interest

The authors have no conflicts of interest relevant to this article.

References

1. H. C. Pretty, "Dissecting aneurysm of coronary artery in a woman aged 42," *Brit. Med. J.* **1**, 667 (1931).
2. S. Tsimikas *et al.*, "Spontaneous coronary artery dissection in patients with renal transplantation," *J. Invasive Cardiol.* **11**, 316–321 (1999).
3. K. H. Mortensen *et al.*, "Spontaneous coronary artery dissection: A western Denmark heart registry study," *Catheter. Cardiovasc. Interv.* **74**, 710–717 (2009), doi: 10.1002/ccd.22115.
4. C. J. M. Vrints, "Spontaneous coronary artery dissection," *Heart* **96**, 801–808 (2010), doi: 10.1136/hrt.2008.162073.
5. F. Alfonso *et al.*, "Spontaneous coronary artery dissection: Novel insights on diagnosis and management," *Cardiovasc. Diagn. Ther.* **5**, 133 (2015).
6. W. I. Schievink, "Spontaneous dissection of the carotid and vertebral arteries," *N. Engl. J. Med.* **344**, 898–906 (2001), doi: 10.1056/nejm200103223441206.
7. W. Völker *et al.*, "The outer arterial wall layers are primarily affected in spontaneous cervical artery dissection," *Neurology* **76**, 1463–1471 (2011), doi: 10.1212/wnl.0b013e318217e71c.
8. M. Thomas *et al.*, "Early natural history of spontaneous coronary artery dissection," *Circ. Cardiovasc. Interv.* **11**, e006772 (2018).
9. F. Alfonso *et al.*, "Diagnosis of spontaneous coronary artery dissection by optical coherence tomography," *J. Am. Coll. Cardiol.* **59**, 1073–1079 (2012), doi: 10.1016/j.jacc.2011.08.082.
10. M. Paulo *et al.*, "Combined use of OCT and IVUS in spontaneous coronary artery dissection," *JACC Cardiovasc. Imaging* **6**, 830–832 (2013), doi: 10.1016/j.jcmg.2013.02.010.
11. A. Maehara *et al.*, "Intravascular ultrasound assessment of spontaneous coronary artery dissection," *Am. J. Cardiol.* **89**, 466–468 (2002), doi: 10.1016/s0002-9149(01)02272-x.
12. J. Saw, "Coronary angiogram classification of spontaneous coronary artery dissection," *Catheter. Cardiovasc. Interv.* **84**, 1115–1122 (2013), doi: 10.1002/ccd.25293.
13. L. McGrath-Cadell, C. J. Holloway, "Early aftermath of spontaneous coronary artery dissection," *Circ. Cardiovasc. Interv.* **11**, e007237 (2018), doi: 10.1161/circinterventions.118.007237.
14. M. S. Tweet *et al.*, "Multimodality imaging for spontaneous coronary artery dissection in women," *JACC Cardiovasc. Imaging* **9**, 436–450 (2016), doi: 10.1016/j.jcmg.2016.01.009.
15. J. Saw *et al.*, "Angiographic appearance of spontaneous coronary artery dissection with intramural hematoma proven on intracoronary imaging," *Catheter. Cardiovasc. Interv.* **87**, E54–E61 (2015), doi: 10.1002/ccd.26022.
16. B. C. Das Neves *et al.*, "Evolutive recanalization of spontaneous coronary artery dissection: Insights from a multimodality imaging approach," *Circulation* **129**, 719–720 (2014), doi: 10.1161/CIRCULATIONAHA.112.000101.
17. N. Vasile *et al.*, "Computed tomography of thoracic aortic dissection: Accuracy and pitfalls," *J. Comput. Assist. Tomogr.* **10**, 211–215 (1986), doi: 10.1097/00004728-198603000-00008.
18. R. Gebker *et al.*, "Comparison of different MRI techniques for the assessment of thoracic aortic pathology: 3D contrast enhanced MR angiography, turbo spin echo and balanced steady state free precession," *Int. J. Card. Imaging* **23**, 747–756 (2007), doi: 10.1007/s10554-006-9204-6.
19. T. Sommer *et al.*, "Aortic dissection: A comparative study of diagnosis with spiral CT, multiplanar

transesophageal echocardiography, and MR imaging," *Radiology* **199**, 347–352 (1996), doi: 10.1148/radiology.199.2.8668776.
20. F. Alfonso, E. Canales, G. Aleong, "Spontaneous coronary artery dissection: Diagnosis by optical coherence tomography," *Eur. Heart J.* **30**, 385 (2008), doi: 10.1093/eurheartj/ehn441.
21. K. Ishibashi, H. Kitabata, T. Akasaka, "Intracoronary optical coherence tomography assessment of spontaneous coronary artery dissection," *Heart* **95**, 818 (2009), doi: 10.1136/hrt.2008.158485.
22. J.-H. Lee, J.-S. Park, "Optical coherence tomography findings of spontaneous coronary artery dissection after conservative treatment," *Coron. Artery Dis.* **32**, 473–474 (2020), doi: 10.1097/mca.0000000000000936.
23. F. Prati *et al.*, "Expert review document on methodology, terminology, and clinical applications of optical coherence tomography: Physical principles, methodology of image acquisition, and clinical application for assessment of coronary arteries and atherosclerosis," *Eur. Heart J.* **31**, 401–415 (2009), doi: 10.1093/eurheartj/ehp433.
24. W. F. Cheong, S. A. Prahl, A. J. Welch, "A review of the optical properties of biological tissues," *IEEE J. Quantum Electron* **26**, 2166–2185 (1990).
25. L. Yan *et al.*, "Fully integrated optical coherence tomography, ultrasound, and indocyanine green--based fluorescence tri-modality system for intravascular imaging," *Biomed. Opt. Express* **8**, 1036–1044 (2017), doi: 10.1364/BOE.8.001036.
26. Y. Li *et al.*, "Intravascular optical coherence tomography for characterization of atherosclerosis with a 1.7 micron swept-source laser," *Sci. Rep.* **7**, 14525 (2017), doi: 10.1038/s41598-017-15326-4.
27. G. J. Tearney *et al.*, "Three-dimensional coronary artery microscopy by intracoronary optical frequency domain imaging," *JACC Cardiovasc. Imaging* **1**, 752–761 (2008), doi: 10.1016/j.jcmg.2008.06.007.
28. Z. Yaqoob *et al.*, "Methods and application areas of endoscopic optical coherence tomography," *J. Biomed. Opt.* **11**, 063001 (2006), doi: 10.1117/1.2400214.
29. C. H. Li, L. V. Wang, "Photoacoustic tomography and sensing in biomedicine," *Phys. Med. Biol.* **54**, R59–R97 (2009), doi: 10.1088/0031-9155/54/19/R01.
30. P. Wang *et al.*, "Intravascular tri-modality system: Combined ultrasound, photoacoustic, and elasticity imaging," *Appl. Phys. Lett.* **113**, 253701 (2018), doi: 10.1063/1.5051387.
31. L. Wang *et al.*, "Tapered fiber-based intravascular photoacoustic endoscopy for high-resolution and deep-penetration imaging of lipid-rich plaque," *Catheter. Cardiovasc. Interv.* **84**, 1115–1122 (2019).
32. X. Ma *et al.*, "Suppression of reverberations at fiber tips for optical ultrasound sensing," *Opt. Lett.* **45**(9), 2526–2529 (2020).
33. X. Ma *et al.*, "Fiber optic-based laser interferometry array for three-dimensional ultrasound sensing," *Opt. Lett.* **44**(23), 5852–5855 (2019).
34. H. Schulz-Hildebrandt *et al.*, "High-speed fiber scanning endoscope for volumetric multi-megahertz optical coherence tomography," *Opt. Lett.* **43**(18), 4386–4389 (2018).
35. G. J. Tearney *et al.*, "Catheter-based optical imaging of a human coronary artery," *Circulation* **94**, 3013 (1996).
36. M. J. Gora *et al.*, Endoscopic optical coherence tomography: Technologies and clinical applications," *Biomed. Opt. Express* **8**(5), 2405–2444 (2017).
37. Y. Yi *et al.*, "Integrated optical coherence tomography, ultrasound and photoacoustic imaging for ovarian tissue characterization," *Biomed. Opt. Express* **2**, 2551–2561 (2011).
38. S. Liang *et al.*, "Trimodality imaging system and intravascular endoscopic probe combined optical coherence tomography, fluorescence imaging and ultrasound imaging," *Opt. Lett.* **39**, 6652–6655 (2014).
39. X. Dai *et al.*, "Miniature endoscope for multimodal imaging," *ACS Photon.* **4**(1), 174–180 (2017).
40. J. Leng *et al.*, "Multi-spectral intravascular photoacoustic/ultrasound/optical coherence tomography tri-modality system with a fully-integrated 0.9-mm full field-of-view catheter for plaque vulnerability imaging," *Biomed. Opt. Express* **12**(4), 1934–1946 (2021).
41. W. Yuan *et al.*, "Optimal operational conditions for supercontinuum-based ultrahigh-resolution endoscopic OCT imaging," *Opt. Lett.* **41**, 250–253 (2016).
42. W. Yuan *et al.*, "Super-achromatic monolithic microprobe for ultrahigh-resolution endoscopic optical coherence tomography at 800 nm," *Nat. Commun.* **8**, 1531, doi: 10.1038/s41467-017-01494-4 (2017).
43. J. Jose *et al.*, "Imaging of tumor vasculature using Twente photoacoustic systems," *J. Biophoton.* **2**, 701–717 (2009).
44. B. L. Bungart *et al.*, "Photoacoustic tomography of intact human prostates and vascular texture analysis identify prostate cancer biopsy targets," *Photoacoustics* **11**, 46–55 (2018).
45. Laser Institute of America, American National Standard for Safe Use of Lasers ANSI Z136. 1-2014 (2014).
46. K.-X. Qing *et al.*, "Ex-vivo haemodynamic models for the study of stanford type B aortic dissection in

isolated Porcine Aorta," *Eur. J. Vasc. Endovasc. Surg.* **44**, 399–405 (2012).
47. E. M. Faure *et al.*, "Human ex-vivo model of Stanford type B aortic dissection," *J. Vasc. Surg.* **60**, 767–775 (2014).
48. J. Hui *et al.*, "Real-time intravascular photoacoustic-ultrasound imaging of lipid-laden plaque in human coronary artery at 16 frames per second," *Sci. Rep.* **7**, 1417 (2017), doi: 10.1038/s41598-017-01649-9.
49. M. Wu *et al.*, "Real-time volumetric lipid imaging in vivo by intravascular photoacoustic at 20 frames per second," *Biomed. Opt. Express* **8**, 943–953 (2017), doi: 10.1364/BOE.8.000943.
50. A. Durrani *et al.*, "Optical rotary junction incorporating a hollow shaft DC motor for high-speed catheter-based optical coherence tomography," *Opt. Lett.* **45**, 487 (2020), doi: 10.1364/ol.382773.
51. Y. C. Cao *et al.*, "High-sensitivity intravascular photoacoustic imaging of lipid-laden plaque with a collinear catheter design," *Sci. Rep.* **6**, 25236 (2016), doi: 10.1038/srep25236.
52. X. R. Ji *et al.*, "Intravascular confocal photoacoustic endoscope with dual-element ultrasonic transducer," *Opt. Express* **23**, 9130 (2015), doi: 10.1364/oe.23.009130.
53. Y. Li *et al.*, "PMN-PT/Epoxy 1-3 composite based ultrasonic transducer for dual-modality photoacoustic and ultrasound endoscopy," *Photoacoustics* **15**, 100138 (2019).
54. S. Lightman *et al.*, "Vortex-Bessel beam generation by 3D direct printing of an integrated multi-optical element on a fiber tip," *Opt. Lett.* **47**(20), 5248–5251 (2022).
55. I. V. A. K. Reddy, A. Bertoncini, C. Liberale, "3D-printed fiber-based zeroth-and high-order Bessel beam generator," *Optica* **9**(6), 645–651 (2022).